Location-Specific Thickness Patterns in Intermediate Age-Related Macular Degeneration Reveals Anatomical Differences in Multiple Retinal Layers

Matt Trinh,[1,2] Vincent Khou,[1,2] Michael Kalloniatis,[1,2] and Lisa Nivison-Smith[1,2]

[1]Centre for Eye Health, University of New South Wales, Sydney, Australia
[2]School of Optometry and Vision Science, University of New South Wales, Sydney, Australia

PURPOSE. To examine individual retinal layers' location-specific patterns of thicknesses in intermediate age-related macular degeneration (iAMD) using optical coherence tomography (OCT).

METHODS. OCT macular cube scans were retrospectively acquired from 84 iAMD eyes of 84 participants and 84 normal eyes of 84 participants propensity-score matched on age, sex, and spherical equivalent refraction. Thicknesses of the retinal nerve fiber layer (RNFL), ganglion cell layer (GCL), inner plexiform layer (IPL), inner nuclear layer (INL), outer plexiform layer (OPL), outer nuclear layer + Henle's fiber layer (ONL$_{+HFL}$), inner- and outer-segment layers (IS/OS), and retinal pigment epithelium to Bruch's membrane (RPE-BM) were calculated across an 8×8 grid (total $24° \times 24°$ area). Location-specific analysis was performed using cluster$_{(normal)}$ and grid$_{(iAMD)}$-to-cluster$_{(normal)}$ comparisons.

RESULTS. In iAMD versus normal eyes, the central RPE-BM was thickened (mean difference $\pm$ SEM up to 27.45% $\pm$ 7.48%, $P < 0.001$; up to 7.6 SD-from-normal), whereas there was thinned outer (OPL, ONL$_{+HFL}$, and non-central RPE-BM, up to $-6.76\% \pm 2.47\%$, $P < 0.001$; up to -1.6 SD-from-normal) and inner retina (GCL and IPL, up to $-4.83\% \pm 1.56\%$, $P < 0.01$; up to -1.7 SD-from-normal) with eccentricity-based effects. Interlayer correlations were greater against the ONL$_{+HFL}$ (mean $|r| \pm$ SEM 0.19 ± 0.03, $P = 0.14$ to < 0.0001) than the RPE-BM (0.09 ± 0, $P = 0.72$ to < 0.0001).

CONCLUSIONS. Location-specific analysis suggests altered retinal anatomy between iAMD and normal eyes. These data could direct clinical diagnosis and monitoring of AMD toward targeted locations.

Keywords: age-related macular degeneration, clustering, OCT, thickness, topography, anatomy

Age-related macular degeneration (AMD) is typically characterized as an outer retinal degeneration, and, subsequently, early investigative efforts into the anatomy of AMD eyes were focused on the outer retinal layers.[1,2] With the advent of optical coherence tomography (OCT), in vivo quantification of all individual retinal layer thicknesses has become more accessible. A plethora of OCT studies have since reported varying macular thickness changes across the whole retina in the early stages of AMD including the retinal nerve fiber layer (RNFL),[3–6] ganglion cell layer (GCL),[3,6–10] inner plexiform layer (IPL),[4,5,11] inner nuclear layer (INL),[3,4,7,12] outer plexiform layer (OPL),[3,4,7] outer nuclear layer (ONL),[3,4,7,13–16] inner- and outer-segment layers (IS/OS),[3,4,7] and retinal pigment epithelium to Bruch's membrane (RPE-BM).[3,4,16–23]

These studies challenge the pre-existing concept of AMD being a disease only of the outer retina. However, only very few studies to our knowledge have concurrently explored macular thicknesses across all individual retinal layers,[3,4,7] thus limiting extrapolation of results in a holistic context. For example, numerous studies demonstrate reduced GCL thickness in the early stages of AMD,[3,6–9,24,25] but lack of context about whether thickness changes are also evident in the surrounding retinal layers hampers conclusions regarding whether this change may represent postreceptoral degeneration or simply be an isolated epiphenomenon. Knowledge of inter-related, concurrent thickness changes in other individual retinal layers would significantly bolster the anatomical understanding of AMD.

Brandl et al.[4] convincingly demonstrated that there were significant, concurrent thickness differences between AMD in its early stages and normal eyes in individual retinal layers of the macula, depending on location. This finding suggests that location-specific analysis of AMD may provide greater clinical insight into where and what retinal changes may occur. This study, however, only assessed a population above 70 years of age, which limits generalizability. Additionally, this study used the Early Treatment for Diabetic Retinopathy Study (ETDRS) sectors for location-specific analyses, which effectively confines retinal space to nine sectors (and combinations thereof) and assumes perfectly concentric anatomical topography. This is not ideal,

considering known topographical variations in several layers,[26–30] particularly the RNFL, which originates nasally.[31,32] Comparison of ETDRS sectors between diseased and normal eyes may also introduce statistical bias when grouping data from the former according to topography of the latter.[33–36] Further study using more detailed spatial analyses, which accommodates for topographical variations of individual retinal layers of both diseased and normal eyes, could provide greater insight into iAMD anatomy, as well as directing attention toward specific retinal locations that may be useful for clinical diagnosis and monitoring of AMD.

Recently, we developed a method of location-specific OCT analysis using cluster analysis that provides greater spatial detail and less variability than the ETDRS sectors.[37] Spatial clustering involves assigning location-specific data into groups of statistical likeness. Use of this method has enabled the formation of OCT-derived topographical thickness maps for each individual retinal layer.[37] These maps are reflective of retinal neuronal distributions described via histological studies more so than the standard ETDRS sectors, which assume neuronal distribution to be concentric and symmetric around the fovea.[37] Application of the GCL topographical thickness map to iAMD eyes using cluster analysis has subsequently led to observation of unique location-specific patterns of thinned GCL toward the central macula and thickened GCL toward the peripheral macula when compared to normal eyes, both statistically significant and large in magnitude of effect.[24]

Application of cluster analysis to individual retinal layers beyond the GCL has yet to be performed. We hypothesize that analyzing location-specific retinal thicknesses in each individual retinal layer of iAMD versus normal eyes using cluster analysis may likewise reveal unique location-specific patterns yet to be described with more limited spatial templates such as the ETDRS sectors. These spatial patterns of thickness differences can help to ameliorate our understanding of AMD anatomy and guide clinical diagnosis and monitoring of iAMD toward targeted retinal locations.

METHODS

Study Population

Participant data were obtained through retrospective review of records from July 12, 2010, to January 13, 2020, of patients attending the Centre for Eye Health (CFEH) in Sydney, Australia. CFEH is a referral-only clinic providing advanced ocular diagnostic testing and disease management by specially trained optometrists and ophthalmologists.[38] All participants in this study provided prior written informed consent to use of their de-identified data for research in accordance with the Declaration of Helsinki and approved by the Biomedical Human Research Ethics Advisory Panel of the University of New South Wales.

Inclusion criteria for normal eyes were defined as visual acuity better than 0.1 logMAR (20/25 Snellen) for participants younger than 60 years old or 0.2 logMAR (20/32 Snellen) for participants older than 60 years old; intraocular pressure <22 mm Hg in both eyes; and no evidence of macular-involving disease including but not limited to AMD, diabetic retinopathy, and glaucoma, nor any signs of significant macular preretinal abnormalities such as vitreo-macular traction, nor any significant macular intraretinal or subretinal deposits, fluid, pigment, or vascular changes.

Inclusion criteria for iAMD eyes were defined as age of 50 years or older, diagnosis of iAMD,[39] and no evidence of macular-involving disease or significant structural abnormalities as described above unrelated to iAMD. Classification of iAMD was based on fundus photography between at least two nonblinded investigators using a modified Beckman Initiative classification,[39] that is, participants 50 to 54 years of age are still considered to have iAMD if they followed all phenotypic criteria in the classification system (as done so in other notable studies).[40–43] Specifically, eyes were classified as iAMD based on the presence of large drusen (>125 μm) or pigmentary abnormalities with at least medium drusen (63–125 μm), without evidence of late AMD signs such as neovascularization or geographic atrophy. No eyes had reticular pseudodrusen. Scanning laser ophthalmoscopy photography and OCT were used to confirm non-late AMD classification and exclude eyes with other posterior ocular disease.

Propensity-Score Matching

Selection of the included normal and iAMD eyes were performed via propensity-score matching using multivariable logistic regression based on age, sex, and spherical equivalent refraction. Rather than exact matching, which can lead to larger bias due to individuals being unmatched in a limited sample pool,[44,45] potential predictor covariables were balanced between groups via propensity-score matching.[46–49] IAMD eyes were propensity-score matched with normal eyes using fuzzy matching without replacement.[50,51] Iterative random draws were performed with increasing match tolerance until all iAMD eyes were matched with normal eyes. This resulted in relatively balanced propensity-scores (logistic regression predicted probabilities) of 0.46 ± 0.02 (mean ± SEM) and 0.42 ± 0.02, respectively, and propensity-score match tolerance of 0.2.[52]

Image Acquisition and Retinal Layer Segmentation

OCT macular cube scans, covering an area of 8600 μm × 7167 μm or 30° × 25° across 61 B-scans, were acquired with Spectralis SD-OCT (Heidelberg Engineering, Heidelberg, Germany) as previously described.[37,53,54] In the presence of multiple scans per participant, the earliest scan meeting inclusion criteria without significant artefacts and with signal strength above 15dB were selected. Scans were corrected for ocular tilt and automatic segmentation applied to each individual retinal layer using the HRA/Spectralis Viewing Module 6.9.5.0 (Heidelberg Engineering, Heidelberg, Germany).

Segmentation for the RNFL, GCL, IPL, INL, OPL, ONL + Henle's fiber layer (ONL+HFL), IS/OS, and RPE-BM for iAMD eyes were reviewed across all 61 B-scans and corrected where necessary by authors M.T. and V.K. according to previous studies.[37,53,54] One of two randomized blocks of all participants had their scans reviewed independently by M.T. and V.K. Upon completion, scans from the alternate block of participants were then independently reviewed by the other author. Any segmentation adjustments required from the second block review were achieved through discussion and consensus between M.T. and V.K.. All segmentations were agreed upon by M.T. and V.K. after one session of discussion. Manual correction of segmentation for iAMD eyes were performed in approximately 75% of all B-scans with
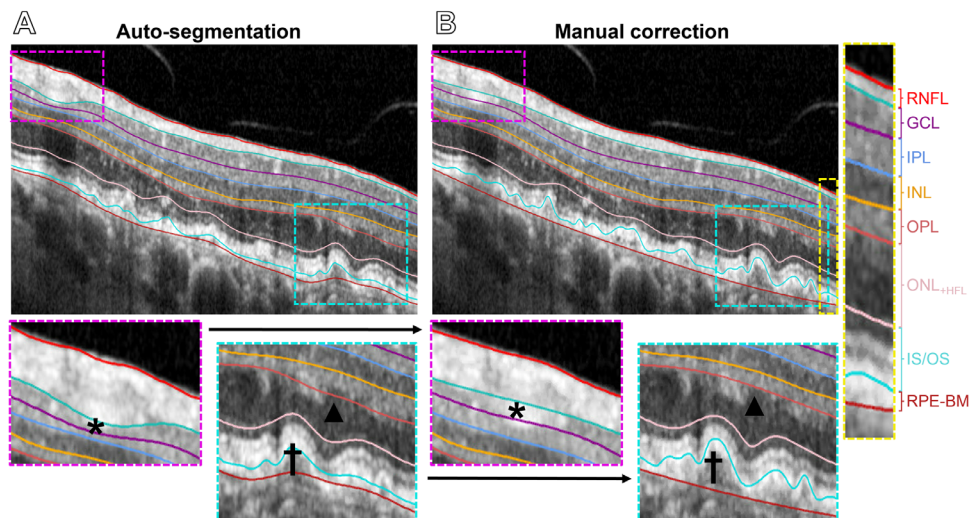
FIGURE 1. Retinal layers segmented within the HRA/Spectralis Viewing Module **(A)** automatically and with **(B)** manual correction. Note the manual correction of segmentation applied to the: distortion surrounding large vasculature (*magenta, asterisk*); ambiguity at Henle's fiber layer (*cyan, arrowhead*); and mis-segmentation surrounding drusen (*cyan, dagger*). The boundaries of each individual retinal layer are displayed in the *yellow* box.

approximately 10% of the contours in each B-scan undergoing minor corrections. Notably, segmentation boundaries were corrected to continue through large vasculature to mitigate their effect on inner retinal layer thicknesses (Figs. 1A, 1B, *magenta, asterisk*), Henle's fiber layer were corrected to be part of the ONL as commonly done so in OCT studies due to its inconsistent reflectivity (despite anatomically being part of the OPL; Figs. 1A, 1B, *cyan, arrowhead*), and mis-segmentation of the inner- and outer-RPE-BM boundaries surrounding drusen were corrected (Figs. 1A, 1B, *cyan, dagger*). Manual correction of segmentation by authors M.T. and V.K. were regarded as the "ground-truth" in concordance with other studies that have compared manual OCT segmentation versus automatic OCT segmentation protocols.[55–57] Manual correction of segmentation for iAMD eyes in this study were performed to the same standard as manual correction of segmentation for normal eyes, which were completed in previous studies.[37,53,54]

Data Extraction

An 8 × 8 grid (total 6880μm × 6880μm or 24° × 24° area) centered on the fovea was placed over macular cube scans (8600 μm × 7167μm or 30° × 25° area). Each grid was 0.74 mm^2 in size (approximately 860 μm × 860 μm or 3° × 3° area). Individual retinal layer thicknesses for iAMD eyes were then extracted as 64 average measurements across the 8 × 8 grid as described from previous studies.[37,53,54] The 8 × 8 grid pattern were selected as it incorporated the highest preset number of B-scans (61 B-scans spaced 120μm apart) using the Spectralis SD-OCT without significant compromise in image quality.[58]

Based on known retinal anatomy, inner retinal cellular displacement and a sharp decline in cellular densities toward the fovea produces highly variable GCL, IPL, INL, and OPL thicknesses. As such, the central four grids of these layers were excluded. The total number of grids analyzed for each layer was 64 in the RNFL, ONL+HFL, IS/OS, and RPE-BM, and 60 in the GCL, IPL, INL, and OPL.

Global Analysis

Global analyses were performed between the total 6880 μm × 6880 μm or 24° × 24° area mean thickness of iAMD versus normal eyes in each individual retinal layer, expressed as mean difference ± SEM in micrometers and as a percentage to account for varying layer thicknesses. To confirm results, multi-variable linear regression including age, sex, spherical equivalent refraction, and AMD status (i.e., iAMD or normal eye) against mean thickness was also performed in each individual retinal layer. Multi-variable linear regression was then repeated using the simplified AREDS severity score[59] instead of AMD status to explore potential dose-response relationships. That is, whether increased AMD severity was associated with greater magnitude of global thickness difference. Scores ranged from zero to two per eye, with one point assigned for the presence of either large drusen or pigmentary abnormalities, and two points assigned for the presence of both.

Location-Specific Analysis

Clusters were predefined as groups of data with statistical likeness, derived from normal OCT grid-wise thicknesses. Normal cluster patterns for each retinal layer formed meaningful, in vivo topographical thickness maps[37,53,54] (Fig. 2A), which corresponded to histological neuronal distributions more so than the standard ETDRS sectors, which assume concentricity and symmetry around the fovea.[37] To address the modifiable areal unit problem (MAUP) for iAMD data, which states that statistical bias may be introduced based on how data are spatially grouped,[34,35] we used two main methods for location-specific analyses: cluster$_{(normal)}$ comparison and grid$_{(iAMD)}$-to-cluster$_{(normal)}$ comparison.

First, cluster$_{(normal)}$ comparison used a more traditional approach to address the MAUP by using spatial grouping that were meaningful and demonstrated inter-group separability and intra-group similarity,[33,34,36] that is, normal clusters.[37,53,54] The mean thickness of iAMD versus normal eyes in each cluster area of each individual retinal layer were
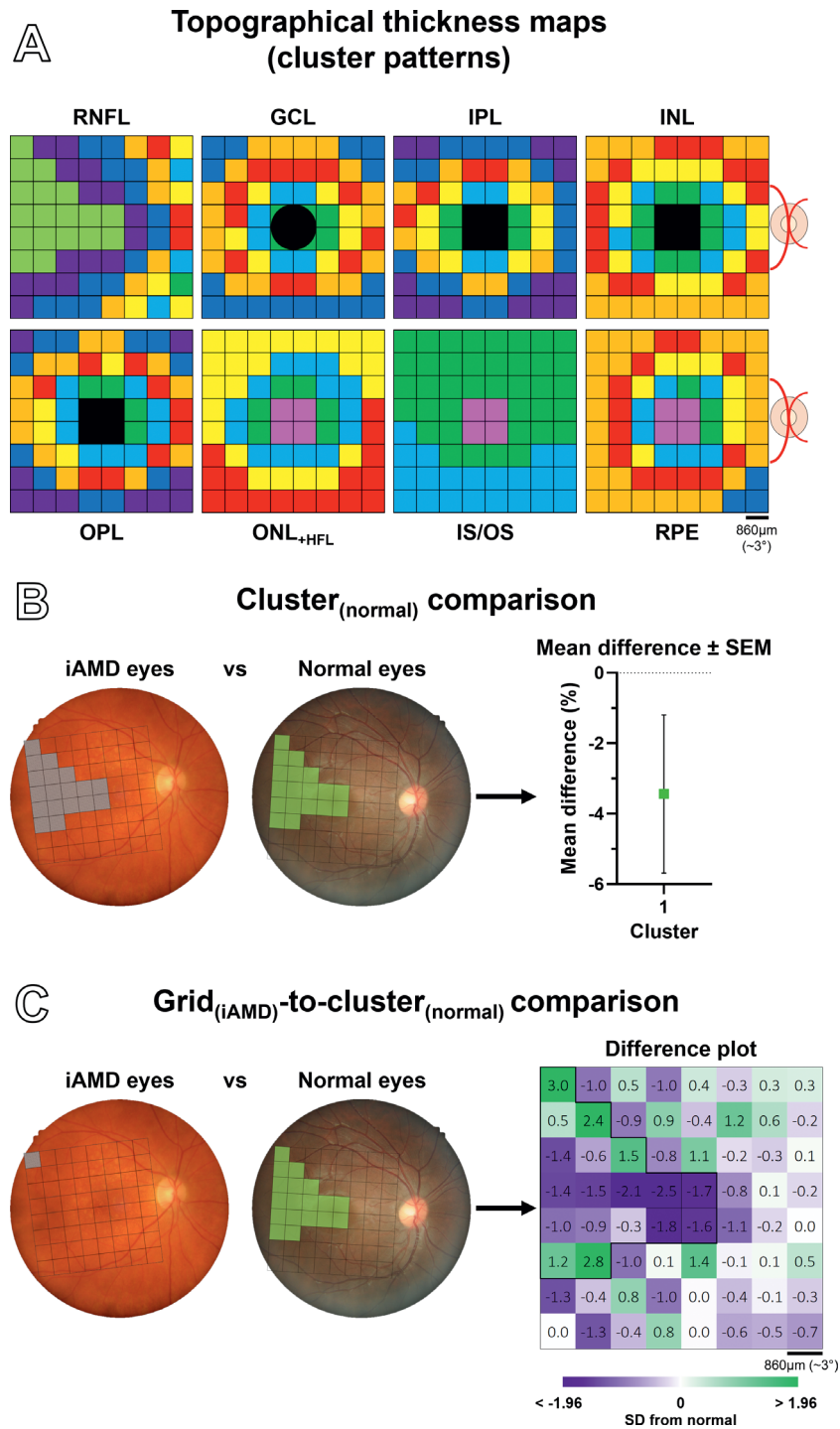
FIGURE 2. Schematic example of location-specific analyses using cluster(normal) and grid(iAMD)-to-cluster(normal) comparisons. **(A)** OCT normative topographical thickness maps for each individual retinal layer, whereby each cluster is represented by a distinct color and defines groups of location-specific data with statistical likeness. **(B)** Cluster(normal) comparison was performed by comparing mean thickness within each cluster area of each individual retinal layer between iAMD versus normal eyes, expressed as mean difference ± SEM. **(C)** Grid(iAMD)-to-cluster(normal) comparison was performed for further spatially detailed analysis, comparing individual grid-wise thicknesses of iAMD eyes to mean cluster thicknesses of normal eyes from the same 10-yearly age group and forming qualitative and quantitative difference plots from normal. Size scale and color scale at the *bottom right*. All images are in right eye format as demonstrated by location of the optic nerve.

expressed as mean difference ± SEM in μm and as a percentage (Fig. 2B). To determine a potential effect of eccentricity on mean differences between iAMD versus normal eyes, a linear regression slope was calculated between each individual retinal layer's mean difference values versus mean eccentricity (°) of each cluster, with exception of the RNFL.

Second, grid$_{(iAMD)}$-to-cluster$_{(normal)}$ comparison further addressed the MAUP by using unmodifiable basic grouping of iAMD data,[34,36] that is, grids, and provided even greater spatial detail and measure of effect sizes (i.e., the strength of a relationship in practical terms).[60–62] Individual grid-wise thicknesses of iAMD eyes were compared to corresponding mean cluster thicknesses of normal eyes from the same 10-yearly age group (Fig. 2C). For example, a 63-year-old participant with iAMD would have each grid-wise thickness compared with the 60- to 69-year-old normal group's corresponding mean cluster thicknesses. Qualitative and quantitative difference plots from normal were formed for each iAMD eye, represented in SD units to account for varying thicknesses across the macula in each retinal layer. Values of 1.96 SD were selected as scale endpoints to represent measurements outside the 95% distribution limits (top and bottom 2.5% of thickness values from normal).

To confirm results derived from comparison of propensity-score matched groups, multivariable linear regression including age, sex, spherical equivalent refraction, and AMD status against mean thickness was performed in each cluster in each individual retinal layer. Multivariable linear regression was repeated using the simplified AREDS severity score[59] instead of AMD status to explore potential location-specific dose-response relationships.

Interlayer Correlation Analysis

To examine whether a rudimentary spatial model could be formed linking the retinal layers of iAMD eyes, we performed grid-to-grid correlational analysis between layers that showed spatial patterns of SD-from-normal thickness differences. To account for Henle's fibers' displacement, the mean eccentricity (mm) of each grid (Supplementary Fig. S1A) alongside additional displacements to these eccentricities according to Drasdo et al.[63] (Supplementary Fig. S1B) were calculated. Comparisons between the outer and inner retinal grids were then adjusted (Supplementary Figs. S1C, S1D), that is, the central four grids of the outer retinal layers would be correlated against the paracentral four grids of the GCL and IPL along the same angular plane from the fovea.

Statistical Analysis

Statistical analyses were performed using GraphPad Prism Version 8, SPSS Version 25, and Microsoft Excel Version 2012. Default significance was considered as $P < 0.05$. Single comparisons between continuous variables were performed using the Student's t-test or Mann-Whitney U-test, depending on the relevant data assumptions. Multiple cluster$_{(normal)}$ comparisons were not adjusted because each comparison was considered important[64] and instead contextualized alongside grid$_{(iAMD)}$-to-cluster$_{(normal)}$ and multivariable linear regression analyses. Single comparisons between categorical variables were performed using Fisher's exact test where available or χ^2 test. SD-from-normal were interpreted according to Cohen's effect sizes, that is, ≥ 0.2 = small, ≥ 0.5 = medium, and ≥ 0.8 = large.[62] Multivariable linear regression analyses were performed with backward stepwise elimination, removing nonsignificant covariables from the regression model in a stepwise manner until all remaining variables were $P < 0.1$ to allow transparency of β values with borderline significance ($0.05 \leq P < 0.1$).[65] Dichotomous values, that is, females and males, AMD status, and normal eye status, were encoded as 1 and 0, respectively.

Correlational analyses were performed using Pearson's r.[62] Multiple comparisons between correlations were performed using Brown-Forsythe and Welch ANOVA for unequal SDs or one-way ANOVA and Tukey's multiple comparisons test for equal SDs.

RESULTS

Participant Demographics

Eighty-four eyes with iAMD from 84 participants and 84 normal eyes from 84 participants were propensity-score matched and included in this study. There were no significant differences with means or distributions of age, sex, spherical equivalent refraction, or visual acuity between the two groups when compared in total or as 10-yearly age groups (Table 1). To explore potential dose-response relationships, further subdivision of the 84 iAMD eyes into simplified AREDS severity scores revealed 60 eyes with a score of one (presence of large drusen or pigmentary abnormalities) and 24 eyes with a score of two (presence of large drusen and pigmentary abnormalities).

Global Analysis in All Retinal Layers

To first determine whether there were differences in total macular thickness between iAMD and normal eyes, each individual retinal layer's total mean thickness (across the total 24° × 24° area) was compared between groups. The mean difference between iAMD and normal eyes showed a significantly thinned mean GCL (-5.03 ± 1.41 %, $P < 0.0001$), IPL (-5.93 ± 1.4 %, $P < 0.0001$), OPL ($-8.36\% \pm 1.16\%$; $P < 0.0001$), and ONL$_{+HFL}$ ($-4.08\% \pm 1.53\%$; $P < 0.01$), whereas the RPE-BM were significantly thickened ($11.55\% \pm 2.11\%$; $P < 0.0001$). There were no significant differences in RNFL, INL, and IS/OS thicknesses between iAMD and normal eyes (Fig. 3).

Multivariable linear regression adjusted for all covariables in propensity score matching (age, sex, and spherical equivalent refraction) showed that AMD status was significantly associated with mean thickness in the GCL ($\beta = 1.27$ [0.47, 2.07]; $P < 0.01$), IPL ($\beta = 1.29$ [0.63, 1.96]; $P < 0.0001$), OPL ($\beta = 2.2$ [1.6, 2.79]; $P < 0.0001$), ONL$_{+HFL}$ ($\beta = 2$ [0.32, 3.69]; $P < 0.05$), and RPE ($\beta = -1.56$ [$-2.12, -1$]; $P < 0.0001$; Supplementary Table S1). Repeated multivariable linear regression using a simplified AREDS severity score instead of AMD status confirmed the significant associations between AMD with GCL, IPL, OPL, ONL$_{+HFL}$, and RPE-BM global thicknesses (Supplementary Table S3). There was greater slope with increased AMD severity in some layers (notably the RPE-BM) suggesting potential dose-response relationships, although statistical comparisons between slopes of severity scores were precluded because of limited sample size.

Location-Specific Analysis in the RNFL and GCL

Location-specific analysis (for each 3° × 3° grid in the 24° × 24° area) was then performed in each individual retinal layer to assess spatial distribution of retinal thicknesses. In the RNFL, cluster$_{(normal)}$ comparison was performed, whereby the mean thickness within each cluster area derived from the topographical thickness map (Fig. 4A) between iAMD and normal eyes were compared. This demonstrated thinned RNFL in most clusters for iAMD versus normal eyes (-2.61%

Table 1. Normal and iAMD Participant Demographics

	Normal	Intermediate AMD	*P* Value
Eyes, n			
Total	84	84	—
50–59	30	17	
60–69	33	42	0.08[*]
70+	21	25	
Age (years)			
Total	64.09 ± 8.34	66.12 ± 7.12	0.09[†]
50–59	55.7 ± 2.5	55.87 ± 3.09	0.84[‡]
60–69	64.27 ± 2.97	65.38 ± 2.54	0.08[‡]
70+	75.8 ± 3.98	74.33 ± 3.53	0.19[‡]
Sex (females/males)			
Total	51:33	51:33	1[§]
50–59	23:7	13:4	>0.99[§]
60–69	20:13	30:12	0.34[§]
70+	8:13	8:17	0.76[§]
Spherical equivalent refraction (diopters)			
Total	0.52 ± 1.22	0.74 ± 1.8	0.36[†]
50–59	0.23 ± 0.71	0.47 ± 0.53	0.23[‡]
60–69	0.51 ± 1.53	0.32 ± 2	0.65[‡]
70+	0.96 ± 1.17	1.62 ± 1.68	0.14[‡]
VA (logMAR)			
Total	0.05 ± 0.1	0.06 ± 0.1	0.71[†]
50–59	0 ± 0.05	0 ± 0.03	0.73[‡]
60–69	0.51 ± 1.53	0.32 ± 2	0.65[‡]
70+	0.96 ± 1.17	1.62 ± 1.68	0.14[‡]

VA, visual acuity (aided).

Continuous values are expressed as mean ± standard deviation (SD). Categorical values are expressed as counts. Normal and iAMD participants' total group and 10-yearly age group data are presented.

[*] χ^2 test.
[†] Student's *t*-test.
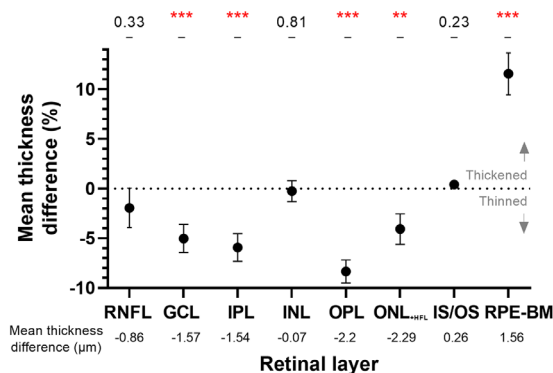[‡] Mann-Whitney *U*-test.
[§] Fisher's exact test.

Figure 3. Global analysis in each individual retinal layer represented as total mean thickness difference (%) ± SEM of iAMD versus normal eyes. *P* values are noted above data points. Significant *P* values are denoted by: *$P < 0.05$, **$P < 0.01$, ***$P < 0.001$.

± 2.24% to −0.03% ± 2.37%; Fig. 4B). No differences in any cluster, however, reached statistical significance.

Grid$_{(iAMD)}$-to-cluster$_{(normal)}$ comparison was then performed, whereby grid-wise thicknesses of iAMD eyes were compared to corresponding mean cluster thicknesses of normal eyes from the same 10-yearly age group. The resultant difference plot confirmed a scattered distribution of thickness differences in the RNFL (Fig. 4C). Although some locations demonstrated a large magnitude of thinned

and thickened RNFL (−2.5 SD- to 3 SD-from-normal), there was no distinguishable spatial pattern of differences.

In the GCL, cluster$_{(normal)}$ comparison using the topographical thickness map (Fig. 4D) displayed thinned GCL in clusters 1 to 4 for iAMD versus normal eyes (−4.37% ± 1.63% to −3.74% ± 1.61%; $P < 0.01$ to $P < 0.05$; Fig. 4E). Differences in the peripheral macula clusters 5 and 6 did not reach statistical significance. Linear regression slope of GCL mean differences versus mean eccentricity (°) of each cluster were calculated. The linear regression was significant ($\beta = 0.38 ± 0.09$, $P < 0.05$; Supplementary Table S2), implying decreased magnitude of thinned GCL with increasing retinal eccentricity.

Grid$_{(iAMD)}$-to-cluster$_{(normal)}$ comparison of the GCL of iAMD versus normal eyes confirmed up to a large magnitude of thinned GCL across most macula locations (up to −1.7 SD-from-normal). Some locations toward the peripheral macula, particularly inferiorly, demonstrated large magnitude of thickened GCL (up to 1.1 SD-from-normal; Fig. 4F).

Multivariable linear regression adjusted for age, sex, and spherical equivalent refraction showed that AMD status were significantly associated with thicknesses in GCL clusters 1 to 5 ($\beta = −3.51$ [−5.01, −2.01] to −0.77 [−1.45, −0.09]; $P < 0.0001$ to $P < 0.05$), and no clusters in the RNFL (Supplementary Table S3). Repeated multivariable linear regression using a simplified AREDS severity score confirmed the associations between AMD GCL clusters 1 to 5 thicknesses (score 1 $\beta = −3.09$ [−4.73, −1.45] to −0.71 [−1.46, 0.04], $P < 0.001$ to $P < 0.1$; score 2 $\beta = −4.54$ [−6.78, −2.31] to −0.91 [−1.94, 0.11], $P < 0.0001$ to $P < 0.1$; Supplementary
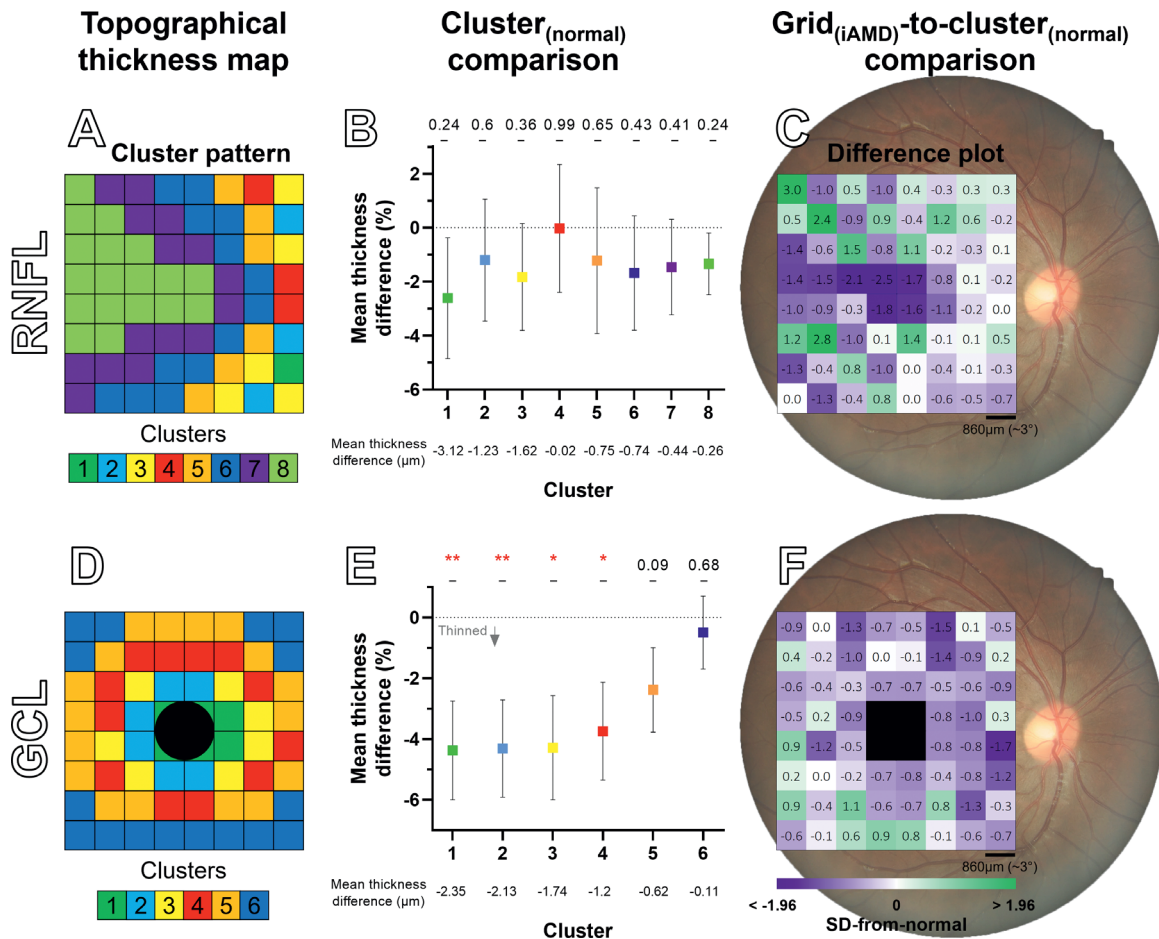
FIGURE 4. Location-specific analysis in the RNFL and GCL. Previously developed topographical thickness maps in the **(A)** RNFL and **(D)** GCL are represented by spatial clusters of distinct colors, whereby clusters are in order of greatest to lowest mean thicknesses (color scale *below*). Central black shading in the GCL represents the excluded area containing the fovea. Cluster$_{(normal)}$ comparison of iAMD versus normal eyes in the **(B)** RNFL and **(E)** GCL are displayed via mean difference (%) graphs ± SEM. Mean difference values in µm are included below the *x*-axis. *P* values are noted above data points. Significant *P* values are denoted by **P* < 0.05, ***P* < 0.01. Grid$_{(iAMD)}$-to-cluster$_{(normal)}$ comparison of iAMD versus normal eyes in the **(C)** RNFL and **(F)** GCL are displayed via difference plots in SD units. Size scale and color scale at the *bottom right*. All images are in right eye format as demonstrated by location of the optic nerve in the underlying fundus photo.

Table S3), and almost no RNFL clusters. There was consistently greater slope with increased AMD severity in GCL clusters 1 to 5, which may have indicated a dose-response relationship.

Location-Specific Analysis in the IPL, INL, and OPL

In the IPL, cluster$_{(normal)}$ comparison indicated thinned IPL in clusters 1 to 5 in iAMD versus normal eyes (−4.83% ± 1.56% to −3.42% ± 1.56%; *P* < 0.01 to *P* < 0.05; Figs. 5A, 5B). Differences in the peripheral macular clusters 6 and 7 did not reach statistical significance. The linear regression slope of all IPL clusters was non-significant ($\beta = 0.2 \pm 0.08$, *P* = 0.07; Supplementary Table S2), implying no significant effect of eccentricity on IPL thicknesses in iAMD eyes versus normal eyes.

Grid$_{(iAMD)}$-to-cluster$_{(normal)}$ comparison confirmed thinned IPL across most locations with up to −1.3SD-from-normal (Fig. 5C). Consistent with the linear regression analysis, some locations toward the peripheral macula showed up

to large magnitude of thickened IPL (up to 0.8 SD-from-normal).

Meanwhile, the INL cluster$_{(normal)}$ comparison showed nonsignificant mean thickness differences of iAMD versus normal eyes in all clusters (−0.99% ± 1.33% to −0.2% ± 1.22%; Figs. 5D, 5E). The linear regression slope of all INL clusters was also nonsignificant ($\beta = 0.05 \pm 0.05$; *P* = 0.37; Supplementary Table S2).

Grid$_{(iAMD)}$-to-cluster$_{(normal)}$ comparison of iAMD versus normal eyes indicated a scattered distribution of up to medium magnitude of thinned INL (up to −1 SD-from-normal) and up to large magnitude of thickened INL (up to 1.3 SD-from-normal) forming no distinguishable spatial pattern (Fig. 5F).

In the OPL, cluster$_{(normal)}$ comparison revealed thinned OPL in all clusters (−6.76% ± 2.47% to −3.16% ± 1.02%; *P* < 0.001 to *P* < 0.01). The linear regression slope of all OPL clusters was significant ($\beta = 0.38 \pm 0.03$; *P* < 0.0001; Supplementary Table S2) and implied less magnitude of thinned OPL with increasing retinal eccentricity.

Grid$_{(iAMD)}$-to-cluster$_{(normal)}$ comparison confirmed up to large magnitude of diffusely thinned OPL (up to −1.5 SD-
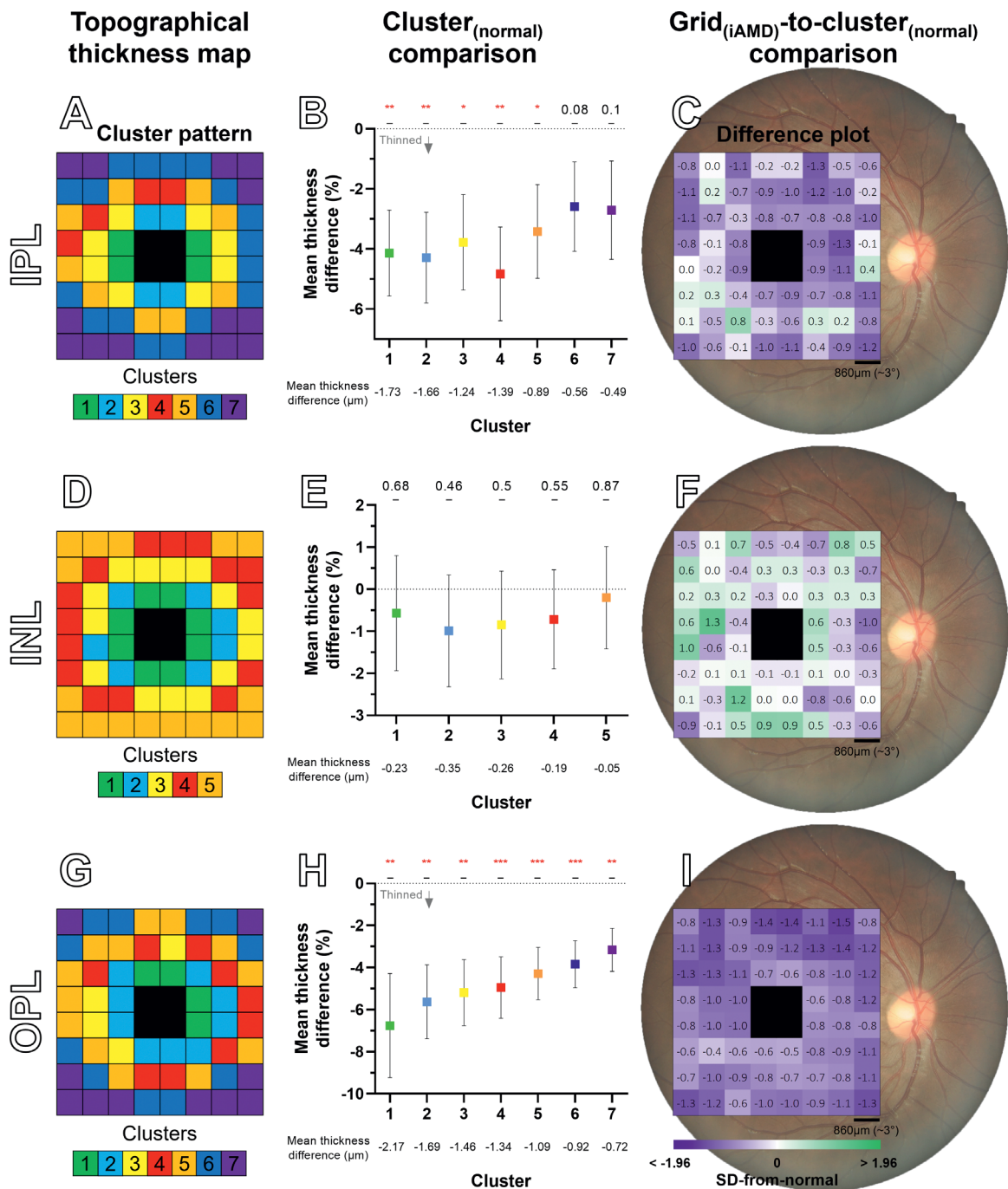
FIGURE 5. Location-specific analysis in the IPL, INL, and OPL. Presentation as in Figure 4. Previously developed topographical thickness maps are displayed for the **(A)** IPL, **(D)** INL, and **(G)** OPL. Cluster comparison of iAMD versus normal eyes are displayed for the **(B)** IPL, **(E)** INL, and **(H)** OPL. Significant *P* values are denoted by ***P < 0.001, ****P < 0.0001. Grid(iAMD)-to-cluster(normal) comparison of iAMD versus normal eyes are displayed for the **(C)** IPL, **(F)** INL, and **(I)** OPL.

from-normal; Fig. 5I), although the aforementioned slope describing less thinned OPL with increasing eccentricity was not appreciable likely because of intercluster differences in SD.

Multivariable linear regression adjusted for age, sex, and spherical equivalent refraction showed that AMD status were significantly associated with thicknesses in all IPL clusters ($\beta = -2.58$ [-3.56, -1.61] to -0.74 [-1.36, -0.12]; $P < 0.0001$ to 0.05), all OPL clusters ($\beta = -3.99$ [-5.58,

-2.4] to -1.26 [-1.69, -0.83], $P < 0.0001$), and no INL clusters (Supplementary Table S3). Repeated multivariable linear regression using a simplified AREDS severity score confirmed the associations between AMD with all IPL and OPL cluster thicknesses (scores 1 and 2 $\beta = -4.4$ [-6.79, -2.01] to -0.78 [-1.46, -0.09], $P < 0.0001$ to $P < 0.05$; Supplementary Table S3), and no INL clusters. However, there appeared to be no consistent patterns of dose-response relationships in these layers.
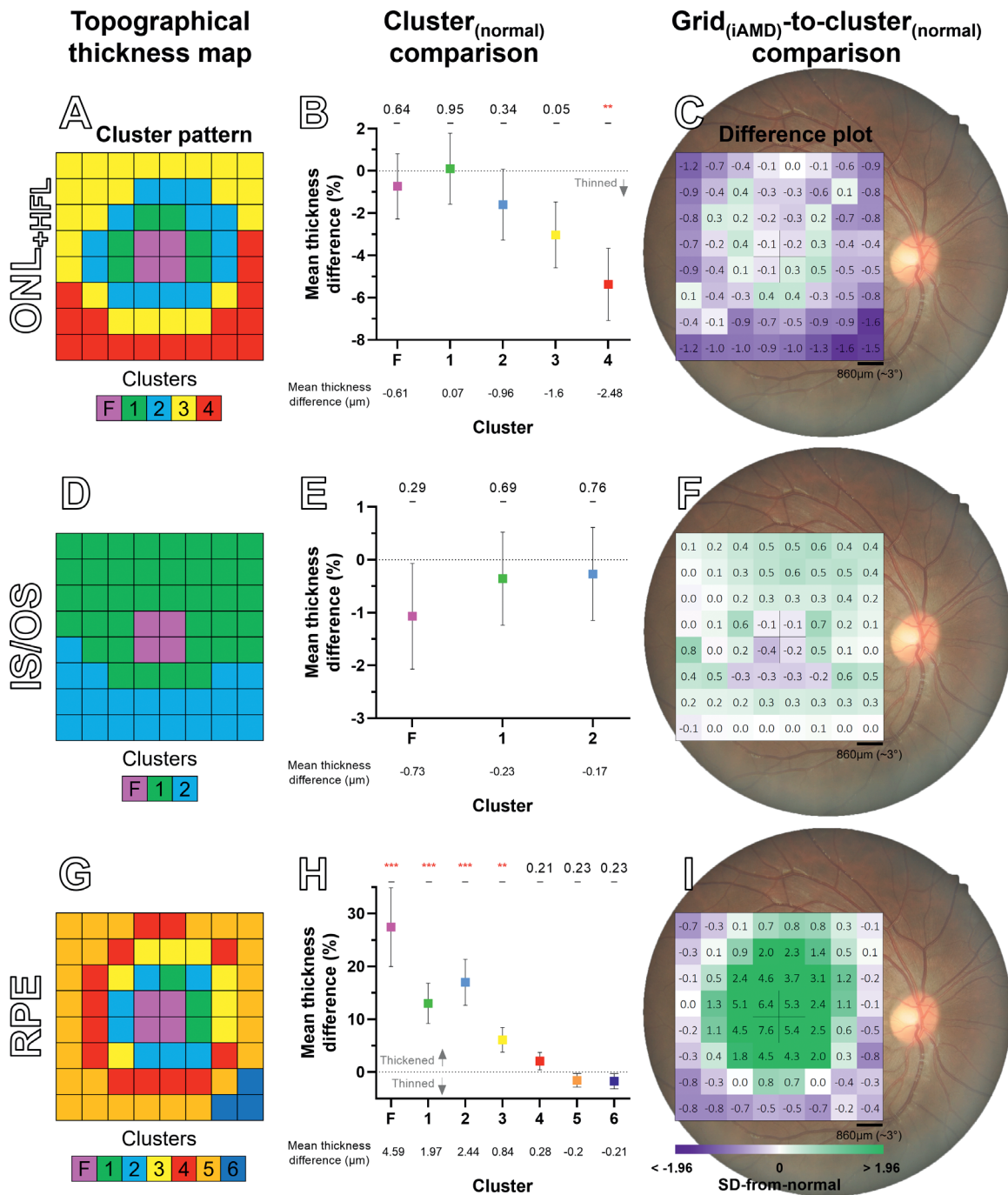
FIGURE 6. Location-specific analysis in the ONL_{+HFL}, IS/OS, and RPE-BM. Presentation as in Figure 4. Previously developed topographical thickness maps are displayed for the **(A)** ONL_{+HFL}, **(D)** IS/OS, and **(G)** RPE-BM. $Cluster_{(normal)}$ comparison of iAMD versus normal eyes are displayed for the **(B)** ONL_{+HFL}, **(E)** IS/OS, and **(H)** RPE-BM. Significant *P* values are denoted by: ***$P < 0.001$, ****$P < 0.0001$. $Grid_{(iAMD)}$-to-cluster$_{(normal)}$ comparison of iAMD versus normal eyes are displayed for the **(C)** ONL_{+HFL}, **(F)** IS/OS, and **(I)** RPE-BM. F, foveal.

Location-Specific Analysis in the ONL_{+HFL}, IS/OS, and RPE-BM

The ONL_{+HFL} cluster$_{(normal)}$ comparison displayed nonsignificant mean differences of iAMD versus normal eyes in the foveal cluster and clusters 1 and 2 ($-1.6\% \pm 1.68\%$ to $0.1\% \pm 1.68\%$). The ONL_{+HFL} was borderline thinned in peripheral macula cluster 3 ($-3.03\% \pm 1.56\%$; $P = 0.05$) and significantly thinned in peripheral macula cluster 4 ($-5.37\% \pm 1.71\%$; $P < 0.01$; Figs. 6A, 6B). Linear regression slope of

all ONL_{+HFL} clusters was significant ($\beta = -0.47 \pm 0.14$; $P < 0.05$; Supplementary Table S2), implying greater magnitude of thinned ONL_{+HFL} with increasing retinal eccentricity.

$Grid_{(iAMD)}$-to-cluster$_{(normal)}$ comparison toward the central macula of iAMD eyes highlighted small magnitude of thinned ONL_{+HFL} (up to -0.3SD-from-normal) and up to medium magnitude of thickened ONL_{+HFL} (up to 0.5 SD-from-normal). At the peripheral macula, there were up to large magnitude of thinned ONL_{+HFL} (up to -1.6 SD-from-normal; Fig. 6C).

TABLE 2. Correlations Between Inter-Layer SD-From-Normal Thickness Differences

	RPE-BM	ONL$_{+HFL}$	OPL	IPL
ONL$_{+HFL}$	0.1 ± 0.01 (7/64)	—	—	—
OPL	0.09 ± 0.01 (3/60)	0.24 ± 0.02 (29/60)	—	—
IPL	0.08 ± 0.01 (1/64)	0.14 ± 0.01 (16/64)	0.12 ± 0.01 (6/60)	—
GCL	0.1 ± 0.01 (5/64)	0.19 ± 0.01 (26/64)	0.12 ± 0.01 (11/60)	0.58 ± 0.02 (61/64)
Mean	0.09 ± 0	0.19 ± 0.03	0.12 ± 0	—

Values are expressed as |r| mean ± SEM (and number of significant grid correlations). Note that the IPL and GCL have 64 grid correlations (rather than 60) after adjustment for displacements according to Drasdo et al.[63]

In the IS/OS, cluster$_{(normal)}$ comparison exhibited no significant differences in any cluster for iAMD versus normal eyes (Figs. 6D, 6E). Linear regression of IS/OS mean differences versus mean eccentricity (°) of each cluster were also nonsignificant ($\beta = 0.09 \pm 0.01$; $P = 0.08$; Supplementary Table S2).

Grid$_{(iAMD)}$-to-cluster$_{(normal)}$ comparison demonstrated small magnitude of thinned IS/OS toward the central macula (up to −0.4SD-from-normal) and the up to large magnitude of thickened IS/OS toward the peripheral macula (up to 0.8 SD-from-normal; Fig. 6F) of iAMD versus normal eyes.

Finally in the RPE-BM, cluster$_{(normal)}$ comparison showed significantly thickened RPE-BM centrally in the foveal cluster and clusters 1 to 3 (27.45% ± 7.48% to 6.11% ± 2.33%; $P <$ 0.001 to $P < 0.01$; Figs. 6G, 6H). No differences in clusters 4 to 6 reached statistical significance. Linear regression of RPE-BM mean differences versus mean eccentricity (°) of each cluster was significant ($\beta = -2.53 \pm 0.39$; $P < 0.01$; Supplementary Table S2), implying reduced thickening of the RPE-BM with increasing retinal eccentricity.

Grid$_{(iAMD)}$-to-cluster$_{(normal)}$ comparison was consistent with the linear regression analysis, demonstrating a large magnitude of thickened RPE-BM toward the central macula (up to 7.6 SD-from-normal) and up to large magnitude of thinned RPE-BM toward the peripheral macula (up to −0.8 SD-from-normal; Fig. 6I) for iAMD eyes.

Multivariable linear regression adjusted for age, sex, and spherical equivalent refraction showed that AMD status was associated with cluster thicknesses in ONL$_{+HFL}$ clusters 3 and 4 ($\beta = -2.35$ [-4, −0.71] and −4.29 [−5.83, −2.75]; $P < 0.01$ and < 0.0001, respectively; Supplementary Table S3), and RPE-BM foveal cluster and clusters 1 to 4 ($\beta = 9.43$ [−6.29, 12.57] to 0.73 [−0.22, 1.24]; $P < 0.0001$ to $P < 0.01$). AMD status was not significantly associated with thicknesses in any IS/OS clusters. Repeated multivariable linear regression using a simplified AREDS severity score confirmed the associations between AMD with ONL$_{+HFL}$ clusters 3 and 4 (scores 1 and 2 $\beta = -4.57$ [−6.26, −2.89] to −2.09 [−4.55, 0.38]; $P < 0.0001$ to $P < 0.1$), and RPE-BM foveal cluster and clusters 1-4 (score 1 $\beta = 7.36$ [3.99, 10.72] to 1.45 [0.61, 2.28]; $P < 0.0001$ to $P < 0.001$; score 2 $\beta = 14.62$ [10.01, 19.22] to 1.63 [0.89, 2.37]; $P < 0.0001$; Supplementary Table S3), and no IS/OS clusters. There was a consistently greater slope with increased AMD severity in RPE-BM foveal cluster and clusters 1 to 4, which may have indicated a dose-response relationship.

Correlating Interlayer Thickness Differences in iAMD

Finally, we examined whether a rudimentary spatial model could be formed linking the retinal layers of iAMD eyes that showed spatial patterns of SD-from-normal thickness differences. Grid-to-grid correlations between the RPE, ONL$_{+HFL}$, OPL, IPL, and GCL were performed after adjustment for Henle's fibers' displacement regarding the GCL and IPL (Supplementary Fig. S1). Absolute correlations significantly varied between comparisons (Brown-Forsythe and Welch ANOVA; $P < 0.0001$; Table 2). As expected, the IPL and GCL had the greatest absolute correlation (|r| ± SEM; 0.58 ± 0.02, 61/64 grids significant), followed by the ONL$_{+HFL}$ and OPL (0.24 ± 0.02, 29/60 grids significant). The ONL$_{+HFL}$ provided the next greatest absolute correlations, albeit weak (mean |r| ± SEM; 0.19 ± 0.03; Tukey's multiple comparisons test $P = 0.14$ to $P < 0.0001$), whereas comparisons against the RPE-BM resulted in the poorest absolute correlations (0.09 ± 0; $P = 0.72$ to $P < 0.0001$).

To further investigate the poor correlations using the RPE-BM, we compared the coefficients of variation (CV) within each cluster of the RPE-BM between normal and iAMD eyes. CV were significantly greater in iAMD eyes (mean ± SD, 26.32% ± 16.13%; $P < 0.001$) compared to normal eyes (8.71 ± 0.61 %; Supplementary Table 4), suggesting highly variable levels of drusen load in the iAMD group.

DISCUSSION

In this study, location-specific analyses revealed various patterns of thickness differences between iAMD and normal eyes not evident in global analyses. These difference patterns were unique to each individual retinal layer and exhibited statistical significance or large effect sizes in all individual retinal layers. Results were also mostly in concordance with other OCT studies that have described thickness differences between iAMD versus normal eyes individually in the GCL,[3,6–10] IPL,[4,5,11] OPL,[3,4,7] ONL$_{+HFL}$,[3,4,7,13–16] IS/OS,[3,4,7] or RPE-BM.[3,4,16–23] Specifically, the RPE-BM was thickened centrally, although there was thinned outer (OPL, ONL$_{+HFL}$, and RPE-BM) and inner retina (GCL and IPL) with some eccentricity-based effects. There were significant but weak correlations between the outer and inner retinal layers. These results improve anatomical understanding of iAMD and could guide clinical diagnosis and monitoring of AMD by indicating specific retinal locations more subject to change.

Location-Specific Thickness Analysis Highlights iAMD Anatomy

Our results demonstrated concurrent thickness differences in the outer and inner retinal layers of iAMD eyes. Based on well-established anatomy of OCT reflectance profiles,[66] plausible anatomical explanations for the observed

location-specific thickness patterns are provided. Specifically, locations of thinned GCL and IPL may represent reduced ganglion cell density in the GCL[67] and ganglion cell synapses in the IPL, whereas thinned ONL and OPL may represent reduced photoreceptor density in the ONL and synaptic terminals and proteins in the OPL.[2,68,69] Thinned RPE-BM toward the peripheral macula may be characteristic of RPE atrophy.[2,70–78] Alternatively, thickened GCL and IPL may reflect Müller cell hypertrophy[79] or neuronal proliferative and migratory changes as seen in outer retinal degeneration,[69,80,81] thickened IS/OS could reflect photoreceptor segment disorganization or translocation,[71,82,83] and centrally thickened RPE-BM would likely represent drusen.[84] Multiple cellular populations per OCT reflective layer can, however, confound interpretations of the underlying cellular structures affected in iAMD. Further work combining our results with other measures of retinal integrity could help strengthen interpretation of alterations in AMD retinal anatomy.

In the GCL, OPL, and ONL_{+HFL}, we also observed eccentricity-based effects that may have been consequential to the greater magnitude of thickened RPE-BM centrally. Greater magnitude of thickened retina toward the peripheral macular GCL and OPL could also reflect hypertrophic glial cells or neuronal migration as commonly seen in other outer retinal degenerative diseases such as retinitis pigmentosa.[79] In particular, Müller cell volumes (including their processes that extend approximately from the inner- to the external-limiting membrane) have been proposed to depend on available space.[85] Thus it is possible that the suggested thickening toward the peripheral macula in several individual retinal layers may reflect Müller cell hypertrophy at areas of greater Müller cell density.[86] Differences between central and peripheral Müller cell morphology and transcriptome[87–89] may also explain thickening toward the peripheral retina, although linkage of these findings in vitro to AMD eyes in vivo is yet to be shown. Alternatively, the ONL_{+HFL} showed greater magnitude of thinned retina toward the peripheral macula. Although this may reflect rod susceptibility in AMD,[27,28,90] as has been explored via structural[2,91–96] and functional[97–102] measures, clinical OCT analyses cannot distinguish rod from cone photoreceptors without further augmentation such as adaptive-optics; further research is warranted.

Proposed Mechanisms for "Sparing" of the RNFL and INL

Location-specific analyses suggested sparing of the RNFL and INL in iAMD eyes compared to normal eyes in concordance with other OCT studies.[3–7] The macular RNFL being genuinely spared in the early stages of AMD may reflect similar finding of radial peripapillary capillary plexus sparing in iAMD eyes.[103] Zucchiatti et al.[9] also established that the RNFL is spared in non-neovascular (early and late atrophic stage) AMD but significantly decreased in neovascular AMD. However, these findings are counterintuitive because implied loss of ganglion cells would also allude to concomitant loss of ganglion cell axons. Alternatively, RNFL sparing may be in part an artefact of high variability in macular RNFL thicknesses. Our $grid_{(iAMD)}$-to-$cluster_{(normal)}$ comparison found locations with variable thickness profiles that were masked by an indistinguishable spatial pattern. Variability in macular RNFL thicknesses may have occurred because of the relatively sparse distribution of ganglion cell axons at the macula.[31,32,104–107] Other reasons for the irregular pattern of RNFL thickness profiles may include subclinical vitreo-macular traction, astrocyte hypertrophy, or Müller cell process proliferation in iAMD.[80,81] Further study is required to determine what cellular structures may be implicated in the RNFL of iAMD eyes, if any.

Sparing of the INL alternatively may be attributed to several factors. Histology studies have revealed a complex array of inner retinal remodeling events secondary to photoreceptor degeneration, including outgrowth of rod bipolar dendrites[108] and horizontal and amacrine cell neurites in hereditary retinal degeneration models[109]; inner INL apoptosis (possibly representing amacrine cells) in non-neovascular AMD eyes[71]; and proliferation and upregulation of Müller cells in non-neovascular AMD eyes.[69,80,81] These epiphenomena have been suggested to occur to maintain synaptic functionality with retracted photoreceptor axons in AMD and stimulate adjacent axonal regeneration.[69,71,80,81,108,109] Studies using rodent models of retinal degeneration have also shown reduced number and impaired functionality of bipolar, horizontal, and amacrine cells[110–113]; increased synaptic activity of bipolar and amacrine cells[114]; bipolar and amacrine cell migration[115,116]; and reorganization of Müller cell processes.[115] Although translatability of results from animal studies to human eyes is equivocal, these models underscore the complex machinations possible within the INL that may explain its variable thickness profiles.

Postreceptoral Degeneration in AMD

An emerging pathophysiological theory in AMD suggests that AMD insults may arise from the outer retina or choroid and then propagate via anterograde degeneration within the inner retina. This process is known as anterograde trans-synaptic or postreceptoral degeneration in AMD.[117,118] Although this theory is well discussed in other OCT studies,[3,5–7,9,10] we provided more holistic insight by examining the spatial relationship between retinal layers rather than focusing only on a few specific retinal layers.[5,6,8–10,12–15,15,17–23,119–135] Correlations were poorest when compared against the RPE-BM, possibly because heterogeneous levels of drusen load in the iAMD group may have spatially unpredictable retinal effects. This unpredictability may be exacerbated by the nonlinear association between drusen load and AMD severity as seen with drusen regression.[136,137] Alternatively, correlations were greater, albeit weak compared against the ONL_{+HFL}. It is possible that the spatial areal unit of sampled thicknesses may have been too large and subsequently hampered correlational values.[33] This was particularly notable when considering that Henle's fibers' displacements are much smaller in size than the $3° \times 3°$ grids.[63] Nonetheless, there is still limited evidence to support the theory of postreceptoral degeneration in AMD and future works using location-specific and longitudinal designs could help clarify this theory.

Limitations

The primary limitation of this study was related to the interpretation of OCT data. Although OCT provides an accessible, in vivo measure of retinal reflectance profiles, the cross-sectional location-specific retinal thickness patterns we describe do not specify which cellular structures are

affected and only imply a possible cause-effect relationship with iAMD. In our repeated multivariable regression models, statistical comparisons between slopes of AREDS severity scores were precluded because of limited sample size. Future works using a larger AMD group with broader severities, and possibly more comprehensive grading such as the (non-simplified) AREDS severity scale,[138] could explore potential dose-response relationships such as the greater magnitude of thinned GCL and thickened RPE-BM with increased AMD severity that we described. Further extension of this work, including longitudinal analysis and direct comparison to other measures of retinal cellular integrity such as adaptive-optics OCT or visual function, could also significantly strengthen the putative cause-effect relationship.[139,140]

Additionally, there were slight discrepancies between our results and those of Brandl et al.[4] and Lamin et al.[3]; they found no significant differences in OPL thickness or volume in contrast to our observations of thinned OPL in iAMD eyes. These studies did not, however, clearly account for Henle's fiber layer during segmentation, which may explain the disparity. Our comparative areal units, that is, normal clusters, were also different to the above studies, which may have contributed to minor discrepancies in results. However, we ensured that our comparative areal units were meaningful and had proven intergroup separability and intragroup similarity[37] to mitigate any potential bias.[33–36]

CONCLUSION

Location-specific analyses of each individual retinal layer revealed various patterns of thickness differences between iAMD and normal eyes not evident in global analyses. The central RPE-BM was thickened, whereas there was thinned outer (OPL, ONL$_{+HFL}$, and non-central RPE-BM) and inner retina (GCL and IPL) with some eccentricity-based effects. There were significant but weak correlations between the thinned outer and thinned inner retinal layers. These results improve anatomical understanding of iAMD and could guide clinical diagnosis and monitoring of AMD by indicating specific retinal locations more subject to change.

References

1. Ambati J, Ambati BK, Yoo SH, Ianchulev S, Adamis AP. Age-related macular degeneration: etiology, pathogenesis, and therapeutic strategies. *Surv Ophthalmol.* 2003;48:257–293.

2. Curcio CA, Medeiros NE, Millican CL. Photoreceptor loss in age-related macular degeneration. *Invest Ophthalmol Vis Sci.* 1996;37:1236–1249.

3. Lamin A, Oakley JD, Dubis AM, Russakoff DB, Sivaprasad S. Changes in volume of various retinal layers over time in early and intermediate age-related macular degeneration. *Eye.* 2019;33:428–434.

4. Brandl C, Brücklmayer C, Günther F, et al. Retinal layer thicknesses in early age-related macular degeneration: results from the German AugUR Study. *Invest Ophthalmol Vis Sci.* 2019;60:1581–1594.

5. Muftuoglu IK, Ramkumar HL, Bartsch DU, Meshi A, Gaber R, Freeman WR. Quantitative analysis of the inner retinal layer thicknesses in age-related macular degeneration using corrected optical coherence tomography segmentation. *Retina.* 2018;38:1478–1484.

6. Borrelli E, Abdelfattah NS, Uji A, Nittala MG, Boyer DS, Sadda SR. Postreceptor neuronal loss in intermediate age-related macular degeneration. *Am J Ophthalmol.* 2017;181:1–11.

7. Savastano MC, Minnella AM, Tamburrino A, Giovinco G, Ventre S, Falsini B. Differential vulnerability of retinal layers to early age-related macular degeneration: evidence by SD-OCT segmentation analysis. *Invest Ophthalmol Vis Sci.* 2014;55:560–566.

8. Yenice E, Şengün A, Soyugelen Demirok G, Turaçlı E. Ganglion cell complex thickness in nonexudative age-related macular degeneration. *Eye.* 2015;29:1076–1080.

9. Zucchiatti I, Parodi MB, Pierro L, et al. Macular ganglion cell complex and retinal nerve fiber layer comparison in different stages of age-related macular degeneration. *Am J Ophthalmol.* 160:2015;602–607.e1.

10. Lee EK, Yu HG. Ganglion cell–inner plexiform layer and peripapillary retinal nerve fiber layer thicknesses in age-related macular degeneration. *Invest Ophthalmol Vis Sci.* 2015;56:3976–3983.

11. Klein R, Meuer SM, Myers CE, et al. Harmonizing the classification of age-related macular degeneration in the three continent AMD consortium. *Ophthalmic Epidemiol.* 2014;21:14–23.

12. Ebneter A, Jaggi D, Abegg M, Wolf S, Zinkernagel MS. Relationship between presumptive inner nuclear layer thickness and geographic atrophy progression in age-related macular degeneration. *Invest Ophthalmol Vis Sci.* 2016;57:OCT299–OCT306.

13. Schuman SG, Koreishi AF, Farsiu S, Jung SH, Izatt JA, Toth CA. Photoreceptor layer thinning over drusen in eyes with age-related macular degeneration imaged in vivo with spectral-domain optical coherence tomography. *Ophthalmology.* 2009;116:488–496.e2.

14. Sadigh S, Luo X, Cideciyan AV, et al. Drusen and photoreceptor abnormalities in African-Americans with intermediate non-neovascular age-related macular degeneration. *Curr Eye Res.* 2015;40:398–406.

15. Rogala J, Zangerl B, Assaad N, Fletcher EL, Kalloniatis M, Nivison-Smith L. In vivo quantification of retinal changes associated with drusen in age-related macular degeneration. *Invest Ophthalmol Vis Sci.* 2015;56:1689–1700.

16. Sassmannshausen M, Zhou J, Pfau M, et al. Longitudinal analysis of retinal thickness and retinal function in eyes with large drusen secondary to intermediate age-related macular degeneration. *Ophthalmol Retina.* 2021;5:241–250.

17. Wu Z, Luu CD, Ayton LN, et al. Optical coherence tomography–defined changes preceding the development of drusen-associated atrophy in age-related macular degeneration. *Ophthalmology.* 2014;121:2415–2422.

18. Nivison-Smith L, Wang H, Assaad N, Kalloniatis M. Retinal thickness changes throughout the natural history of drusen in age-related macular degeneration. *Optom Vis Sci*. 2018;95:648–655.

19. Sassmannshausen M, Steinberg JS, Fimmers R, et al. Structure-function analysis in patients with intermediate age-related macular degeneration. *Invest Ophthalmol Vis Sci*. 2018;59:1599–1608.

20. Ferrara D, Silver RE, Louzada RN, Novais EA, Collins GK, Seddon JM. Optical coherence tomography features preceding the onset of advanced age-related macular degeneration. *Invest Ophthalmol Vis Sci*. 2017;58:3519–3529.

21. Acton JH, Smith RT, Hood DC, Greenstein VC. Relationship between retinal layer thickness and the visual field in early age-related macular degeneration. *Invest Ophthalmol Vis Sci*. 2012;53:7618–7624.

22. Farsiu S, Chiu SJ, O'Connell RV, et al. Quantitative classification of eyes with and without intermediate age-related macular degeneration using optical coherence tomography. *Ophthalmology*. 2014;121:162–172.

23. Wu Z, Cunefare D, Chiu E, et al. Longitudinal associations between microstructural changes and microperimetry in the early stages of age-related macular degeneration. *Invest Ophthalmol Vis Sci*. 2016;57:3714–3722.

24. Trinh M, Tong J, Yoshioka N, Zangerl B, Kalloniatis M, Nivison-Smith L. Macula ganglion cell thickness changes display location-specific variation patterns in intermediate age-related macular degeneration. *Invest Ophthalmol Vis Sci*. 2020;61:2.

25. Lee H-J, Kim M-S, Jo Y-J, Kim J-Y. Ganglion cell–inner plexiform layer thickness in retinal diseases: repeatability study of spectral-domain optical coherence tomography. *Am J Ophthalmol*. 2015;160:283–289.e1.

26. Curcio CA, Allen KA. Topography of ganglion cells in human retina. *J Comp Neurol*. 1990;300:5–25.

27. Lee SCS, Martin PR, Grünert U. Topography of neurons in the rod pathway of human retina. *Invest Ophthalmol Vis Sci*. 2019;60:2848–2859.

28. Curcio CA, Sloan KR, Kalina RE, Hendrickson AE. Human photoreceptor topography. *J Comp Neurol*. 1990;292:497–523.

29. Ahnelt PK, Schubert C, Kübber-Heiss A, Schiviz A, Anger E. Independent variation of retinal S and M cone photoreceptor topographies: a survey of four families of mammals. *Vis Neurosci*. 2006;23:429–435.

30. Curcio CA, Allen KA, Sloan KR, et al. Distribution and morphology of human cone photoreceptors stained with anti-blue opsin. *J Comp Neurol*. 1991;312:610–624.

31. Blumenthal E, Parikh RS, Pe'er J, et al. Retinal nerve fibre layer imaging compared with histological measurements in a human eye. *Eye Lond Engl*. 2007;23:171–5.

32. Frenkel S, Morgan JE, Blumenthal EZ. Histological measurement of retinal nerve fibre layer thickness. *Eye*. 2005;19:491–498.

33. Buzzelli M. Modifiable areal unit problem. *Int Encycl Hum Geogr*. 2020;169–173.

34. Jelinski DE, Wu J. The modifiable areal unit problem and implications for landscape ecology. *Landsc Ecol*. 1996;11:129–140.

35. Wong DWS. The Modifiable Areal Unit Problem (MAUP). In: Janelle DG, Warf B, Hansen K , eds. *WorldMinds: Geographical Perspectives on 100 Problems: Commemorating the 100th Anniversary of the Association of American Geographers 1904–2004*. Netherlands: Springer; 2004:571–575.

36. Dark SJ, Bram D. The modifiable areal unit problem (MAUP) in physical geography. *Prog Phys Geogr Earth Environ*. 2007;31:471–479.

37. Trinh M, Khou V, Zangerl B, Kalloniatis M, Nivison-Smith L. Modelling normal age-related changes in individual retinal layers using location-specific OCT analysis. *Sci Rep*. 2021;11:558.

38. Wang H, Kalloniatis M. Clinical outcomes of the Centre for Eye Health: an intra-professional optometry-led collaborative eye care clinic in Australia. *Clin Exp Optom*. 2021;0:1–10.

39. Ferris III FL, Wilkinson CP, Bird A, et al. Clinical classification of age-related macular degeneration. *Ophthalmology*. 2013;120:844–851.

40. Sleiman K, Veerappan M, Winter KP, et al. Optical coherence tomography predictors of risk for progression to non-neovascular atrophic age-related macular degeneration. *Ophthalmology*. 2017;124:1764–1777.

41. Hallak JA, de Sisternes L, Osborne A, Yaspan B, Rubin DL, Leng T. Imaging, genetic, and demographic factors associated with conversion to neovascular age-related macular degeneration: secondary analysis of a randomized clinical trial. *JAMA Ophthalmol*. 2019;137:738–744.

42. Waldstein SM, Vogl WD, Bogunovic H, Sadeghipour A, Riedl S, Schmidt-Erfurth U. Characterization of drusen and hyperreflective foci as biomarkers for disease progression in age-related macular degeneration using artificial intelligence in optical coherence tomography. *JAMA Ophthalmol*. 2020;138:740–747.

43. Guymer RH, Vogl WD, Bogunovic H, Sadeghipour A, Riedl S, Schmidt-Erfurth U. Proof of concept, randomized, placebo-controlled study of the effect of simvastatin on the course of age-related macular degeneration. *PloS One*. 2013;8:e83759.

44. Rosenbaum PR, Rubin DB. Constructing a control group using multivariate matched sampling methods that incorporate the propensity score. *Am Stat*. 1985;39:33–38.

45. Stuart EA. Matching methods for causal inference: a review and a look forward. *Stat Sci Rev J Inst Math Stat*. 2010;25:1–21.

46. Austin PC. An introduction to propensity score methods for reducing the effects of confounding in observational studies. *Multivar Behav Res*. 2011;46:399–424.

47. Dehejia RH, Wahba S. Propensity score-matching methods for nonexperimental causal studies. *Rev Econ Stat*. 2002;84:151–161.

48. Abadie A, Imbens GW. Matching on the estimated propensity score. *Econometrica*. 2016;84:781–807.

49. Caliendo M, Kopeinig S. Some practical guidance for the implementation of propensity score matching. *J Econ Surv*. 2008;22:31–72.

50. Gu XS, Rosenbaum PR. Comparison of multivariate matching methods: structures, distances, and algorithms. *J Comput Graph Stat*. 1993;2:405–420.

51. Guo S, Fraser M, Chen Q. Propensity score analysis: recent debate and discussion. *J Soc Work Res*. 2020;11:463–482.

52. Lunt M. Selecting an appropriate caliper can be essential for achieving good balance with propensity score matching. *Am J Epidemiol*. 2014;179:226–235.

53. Yoshioka N, Zangerl B, Nivison-Smith L, et al. Pattern recognition analysis of age-related retinal ganglion cell signatures in the human eye. *Invest Ophthalmol Vis Sci*. 2017;58:3086–3099.

54. Tong J, Phu J, Khuu SK, et al. Development of a spatial model of age-related change in the macular ganglion cell layer to predict function from structural changes. *Am J Ophthalmol*. 2019;208:166–177.

55. Tian J, Varga B, Tatrai E, et al. Performance evaluation of automated segmentation software on optical coherence tomography volume data. *J Biophotonics*. 2016;9:478–489.

56. Dodo BI, Li Y, Eltayef K, Liu X. Automatic annotation of retinal layers in optical coherence tomography images. *J Med Syst*. 2019;43:336.

57. Maloca PM, Lee AY, de Carvalho ER, et al. Validation of automated artificial intelligence segmentation of optical coherence tomography images. *PLOS ONE*. 2019;14:e0220063.

58. Heidelberg Engineering GmbH. Spectralis Product Family User Manual Software Version 6.7. 2016.

59. Ferris FL, Davis MD, Clemons TE, et al. A simplified severity scale for age-related macular degeneration: AREDS Report No. 18. *Arch Ophthalmol*. 2005;123:1570–1574.

60. Kazis LE, Anderson JJ, Meenan RF. Effect sizes for interpreting changes in health status. *Med Care*. 1989;27:S178–S189.

61. Angst F, Aeschlimann A, Angst J. The minimal clinically important difference raised the significance of outcome effects above the statistical level, with methodological implications for future studies. *J Clin Epidemiol*. 2017;82:128–136.

62. Cohen J. *Statistical power analysis for the Behavioral sciences*. Mahwah, NJ: Lawrence Erlbaum Associates; 1988.

63. Drasdo N, Millican CL, Katholi CR, Curcio CA. The length of Henle fibers in the human retina and a model of ganglion receptive field density in the visual field. *Vision Res*. 2007;47:2901–2911.

64. Armstrong RA. When to use the Bonferroni correction. *Ophthalmic Physiol Opt J Br Coll Ophthalmic Opt Optom*. 2014;34:502–508.

65. Derksen S, Keselman HJ. Backward, forward and stepwise automated subset selection algorithms: frequency of obtaining authentic and noise variables. *Br J Math Stat Psychol*. 1992;45:265–282.

66. Cuenca N, Ortuño-Lizarán I, Pinilla I. Cellular characterization of OCT and outer retinal bands using specific immunohistochemistry markers and clinical implications. *Ophthalmology*. 2018;125:407–422.

67. Medeiros NE, Curcio CA. Preservation of Ganglion Cell Layer Neurons in Age-Related Macular Degeneration. *Invest Ophthalmol Vis Sci*. 2001;42:795–803.

68. Johnson PT, Brown MN, Pulliam BC, Anderson DH, Johnson LV. Synaptic pathology, altered gene expression, and degeneration in photoreceptors impacted by drusen. *Invest Ophthalmol Vis Sci*. 2005;46:4788–4795.

69. Johnson PT, Lewis GP, Talaga KC, et al. Drusen-associated degeneration in the retina. *Invest Ophthalmol Vis Sci*. 2003;44:4481–4488.

70. Sarks JP, Sarks SH, Killingsworth MC. Evolution of soft drusen in age-related macular degeneration. *Eye*. 1994;8:269–283.

71. Dunaief JL, Dentchev T, Ying G-S, Milam AH. The role of apoptosis in age-related macular degeneration. *Arch Ophthalmol*. 2002;120:1435–1442.

72. Xu GZ, Li WW, Tso MO. Apoptosis in human retinal degenerations. *Trans Am Ophthalmol Soc*. 1996;94:411–431.

73. Golestaneh N, Chu Y, Xiao Y-Y, Stoleru GL, Theos AC. Dysfunctional autophagy in RPE, a contributing factor in age-related macular degeneration. *Cell Death Dis*. 2018;8:e2537–2537.

74. Mitter SK, Song C, Qi X, et al. Dysregulated autophagy in the RPE is associated with increased susceptibility to oxidative stress and AMD. *Autophagy*. 2014;10:1989–2005.

75. Inana G, Murat C, An W, Yao X, Harris IR, Cao J. RPE phagocytic function declines in age-related macular degeneration and is rescued by human umbilical tissue derived cells. *J Transl Med*. 2018;16:63.

76. De S, Rabin DM, Salero E, Lederman PL, Temple S, Stern JH. Human retinal pigment epithelium cell changes and expression of αB-crystallin: a biomarker for retinal pigment epithelium cell change in age-related macular degeneration. *Arch Ophthalmol*. 2007;125:641–645.

77. Bressler NM, Munoz B, Maguire MG, et al. Five-year incidence and disappearance of drusen and retinal pigment epithelial abnormalities. Waterman study. *Arch Ophthalmol*. 1995;113:301–308.

78. Green WR, McDonnell PJ, Yeo JH. Pathologic features of senile macular degeneration. *Ophthalmology*. 1985;92:615–627.

79. Chua J, Nivison-Smith L, Fletcher EL, Trenholm S, Awatramani GB, Kalloniatis M. Early remodeling of Müller cells in the *rd/rd* mouse model of retinal dystrophy: Müller cells in rd mouse retina. *J Comp Neurol*. 2013;521:2439–2453.

80. Madigan MC, Penfold PL, Provis JM, Balind TK, Billson FA. Intermediate filament expression in human retinal macroglia. Histopathologic changes associated with age-related macular degeneration. *Retina*. 1994;14:65–74.

81. Wu KHC, Madigan MC, Billson FA, Penfold PL. Differential expression of GFAP in early v late AMD: a quantitative analysis. *Br J Ophthalmol*. 2003;87:1159–1166.

82. Shelley EJ, Madigan MC, Natoli R, Penfold PL, Provis JM. Cone degeneration in aging and age-related macular degeneration. *Arch Ophthalmol*. 2009;127:483–492.

83. Pow DV, Sullivan RKP. Nuclear kinesis, neurite sprouting and abnormal axonal projections of cone photoreceptors in the aged and AMD-afflicted human retina. *Exp Eye Res*. 2007;84:850–857.

84. Bonilha VL. Age and disease-related structural changes in the retinal pigment epithelium. *Clin Ophthalmol Auckl NZ*. 2008;2:413–424.

85. Chao TI, Grosche J, Biedermann B, et al. Comparative studies on mammalian Müller (retinal glial) cells. *J Neurocytol*. 1997;26:439–454.

86. Distler C, Dreher Z. Glia cells of the monkey retina—II. Müller cells. *Vision Res*. 1996;36:2381–2394.

87. Zhang T, Zhu L, Madigan MC, et al. Human macular Müller cells rely more on serine biosynthesis to combat oxidative stress than those from the periphery. *Elife*. 2019;8:e43598.

88. Too LK, Gracie G, Hasic E, Iwakura JH, Cherepanoff S. Adult human retinal Müller glia display distinct peripheral and macular expression of CD117 and CD44 stem cell-associated proteins. *Acta Histochem*. 2017;119:142–149.

89. Bringmann A, Syrbe S, Görner K, et al. The primate fovea: structure, function and development. *Prog Retin Eye Res*. 2018;66:.

90. Ahnelt PK. The photoreceptor mosaic. *Eye*. 1998;12(Pt 3b):531–540.

91. Godara P, Siebe C, Rha J, Michaelides M, Carroll J. Assessing the photoreceptor mosaic over drusen using adaptive optics and SD-OCT. *Ophthalmic Surg Lasers Imaging Retina*. 2010;41(Suppl):S104–S108.

92. Mrejen S, Sato T, Curcio CA, Spaide RF. Assessing the cone photoreceptor mosaic in eyes with pseudodrusen and soft drusen in vivo using adaptive optics imaging. *Ophthalmology*. 2014;121:545–551.

93. Reumueller A, Schmidt-Erfurth U, Salas M, et al. Three-dimensional adaptive optics–assisted visualization of photoreceptors in healthy and pathologically aged eyes. *Invest Ophthalmol Vis Sci*. 2019;60:1144–1155.

94. Querques G, Kamami-Levy C, Blanco-Garavito R, et al. Appearance of medium–large drusen and reticular

pseudodrusen on adaptive optics in age-related macular degeneration. *Br J Ophthalmol*. 2014;98:1522–1527.

95. Zayit-Soudry S, Duncan JL, Syed R, Menghini M, Roorda AJ. Cone structure imaged with adaptive optics scanning laser ophthalmoscopy in eyes with nonneovascular age-related macular degeneration. *Invest Ophthalmol Vis Sci*. 2013;54:7498–7509.

96. Boretsky A, Khan F, Burnett G, et al. In vivo imaging of photoreceptor disruption associated with age-related macular degeneration: a pilot study. *Lasers Surg Med*. 2012;44:603–610.

97. Flamendorf J, Agrón E, Wong WT, et al. Impairments in dark adaptation are associated with age-related macular degeneration severity and reticular pseudodrusen. *Ophthalmology*. 2015;122:2053–2062.

98. Owsley C, McGwin G, Jackson GR, Kallies K, Clark M. Cone- and rod-mediated dark adaptation impairment in age-related maculopathy. *Ophthalmology*. 2007;114:1728–1735.

99. Owsley C, Jackson GR, Cideciyan AV, et al. Psychophysical evidence for rod vulnerability in age-related macular degeneration. *Invest Ophthalmol Vis Sci*. 2000;41:267–273.

100. Owsley C, McGwin G, Jr, Clark ME, et al. Delayed rod-mediated dark adaptation is a functional biomarker for incident early age-related macular degeneration. *Ophthalmology*. 2016;123:344–351.

101. Jackson GR, Scott IU, Kim IK, Quillen DA, Iannaccone A, Edwards JG. Diagnostic sensitivity and specificity of dark adaptometry for detection of age-related macular degeneration. *Invest Ophthalmol Vis Sci*. 2014;55:1427–1431.

102. Nittala MG, Velaga SB, Hariri A, et al. Retinal sensitivity using microperimetry in age-related macular degeneration in an Amish population. *Ophthalmic Surg Lasers Imaging Retina*. 2019;50:e236–e241.

103. Trinh M, Kalloniatis M, Nivison-Smith L. Radial peripapillary capillary plexus sparing and underlying retinal vascular impairment in intermediate age-related macular degeneration. *Invest Ophthalmol Vis Sci*. 2021;62:2.

104. Cohen MJ, Kaliner E, Frenkel S, Kogan M, Miron H, Blumenthal EZ. Morphometric analysis of human peripapillary retinal nerve fiber layer thickness. *Invest Ophthalmol Vis Sci*. 2008;49:941–944.

105. Blumenthal EZ. Quantifying retinal nerve fiber layer thickness histologically: a novel approach to sectioning of the retina. *Invest Ophthalmol Vis Sci*. 2004;45:1404–1409.

106. Dichtl A, Jonas JB, Naumann GO. Retinal nerve fiber layer thickness in human eyes. *Graefes Arch Clin Exp Ophthalmol*. 1999;237:474–479.

107. Varma R, Skaf M, Barron E. Retinal nerve fiber layer thickness in normal human eyes. *Ophthalmology*. 1996;103:2114–2119.

108. Sullivan RKP, WoldeMussie E, Pow DV. Dendritic and synaptic plasticity of neurons in the human age-related macular degeneration retina. *Invest Ophthalmol Vis Sci*. 2007;48:2782–2791.

109. Fariss RN, Li Z-Y, Milam AH. Abnormalities in rod photoreceptors, amacrine cells, and horizontal cells in human retinas with retinitis pigmentosa. *Am J Ophthalmol*. 2000;129:215–223.

110. Marc RE, Jones BW, Anderson JR, et al. Neural reprogramming in retinal degeneration. *Invest Ophthalmol Vis Sci*. 2007;48:3364–3371.

111. Varela C, Igartua I, De la Rosa E, de la Villa P. Functional modifications in rod bipolar cells in a mouse model of retinitis pigmentosa. *Vision Res*. 2003;43:879–885.

112. Strettoi E, Pignatelli V. Modifications of retinal neurons in a mouse model of retinitis pigmentosa. *Proc Natl Acad Sci USA*. 2000;97:11020–11025.

113. Machida S, Raz-Prag D, Fariss RN, Sieving PA, Bush RA. Photopic ERG negative response from amacrine cell signaling in RCS rat retinal degeneration. *Invest Ophthalmol Vis Sci*. 2008;49:442–452.

114. Dagar S, Nagar S, Goel M, Cherukuri P, Dhingra NK. Loss of photoreceptors results in upregulation of synaptic proteins in bipolar cells and amacrine cells. *LoS ONE*. 2014;9.

115. Sullivan R, Penfold P, Pow DV. Neuronal migration and glial remodeling in degenerating retinas of aged rats and in nonneovascular AMD. *Invest Ophthalmol Vis Sci*. 2003;44:856–865.

116. Marc RE, Jones BW, Watt CB, Vazquez-Chona F, Vaughan DK, Organisciak DT. Extreme retinal remodeling triggered by light damage: implications for age related macular degeneration. *Mol Vis*. 2008;14:782–805.

117. Feigl B, Brown B, Lovie-Kitchin J, Swann P. Functional loss in early age-related maculopathy: the ischaemia postreceptoral hypothesis. *Eye*. 2007;21:689–696.

118. Panneman EL, Coric D, Tran LMD, de Vries-Knoppert WAEJ, Petzold A. Progression of anterograde trans-synaptic degeneration in the human retina is modulated by axonal convergence and divergence. *Neuro-Ophthalmol*. 2019;43:382–390.

119. Iwama D, Tsujikawa A, Ojima Y, et al. Relationship between retinal sensitivity and morphologic changes in eyes with confluent soft drusen. *Clin Experiment Ophthalmol*. 2010;38:483–488.

120. Wu Z, Ayton LN, Luu CD, Guymer RH. Relationship between retinal microstructures on optical coherence tomography and microperimetry in age-related macular degeneration. *Ophthalmology*. 2014;121:1445–1452.

121. Hartmann KI, Gomez ML, Bartsch D-UG, Schuster AK, Freeman WR. Effect of change in drusen evolution on photoreceptor inner segment/outer segment junction. *Retina*. 2012;32:1492–1499.

122. Hartmann KI, Bartsch DU, Cheng L, et al. Scanning laser ophthalmoscope imaging stabilized microperimetry in dry age-related macular degeneration. *Retina*. 2011;31:1323–1331.

123. Querques G, Canouï-Poitrine F, Coscas F, et al. Analysis of progression of reticular pseudodrusen by spectral domain–optical coherence tomography. *Invest Ophthalmol Vis Sci*. 2012;53:1264–1270.

124. Querques G, Querques L, Martinelli D, et al. Pathologic insights from integrated imaging of reticular pseudodrusen in age-related macular degeneration. *Retina*. 2011;31:518–26.

125. Zhang Y, Wang X, Rivero EB, et al. Photoreceptor perturbation around subretinal drusenoid deposits as revealed by adaptive optics scanning laser ophthalmoscopy. *Am J Ophthalmol*. 2014;158:584–596.e1.

126. Spaide RF. Outer retinal atrophy after regression of subretinal drusenoid deposits as a newly recognized form of late Age-related macular degeneration. *Retina*. 2013;33:1800–1808.

127. Landa G, Su E, Garcia PMT, Seiple WH, Rosen RB. Inner segment-outer segment junctional layer integrity and corresponding retinal sensitivity in dry and wet forms of age-related macular degeneration. *Retina Phila Pa*. 2011;31:364–370.

128. Yi K, Mujat M, Park BH, et al. Spectral domain optical coherence tomography for quantitative evaluation of drusen and associated structural changes in

non-neovascular age-related macular degeneration. *Br J Ophthalmol*. 2009;93:176–181.

129. Pappuru RR, Ouyang Y, Nittala MG, et al. Relationship between outer retinal thickness substructures and visual acuity in eyes with dry age-related macular degeneration. *Invest Ophthalmol Vis Sci*. 2011;52:6743–6748.

130. Ko TH, Fujimoto JG, Schuman JS, et al. Comparison of ultrahigh- and standard-resolution optical coherence tomography for imaging macular pathology. *Ophthalmology*. 2005;112:1922.e1–1922.e15.

131. Ramon C, Cardona G, Biarnés M, Ferraro LL, Monés J. Longitudinal changes in outer nuclear layer thickness in soft drusen and reticular pseudodrusen. *Clin Exp Optom*. 2019;102:601–610.

132. Sadigh S, Cideciyan AV, Sumaroka A, et al. Abnormal thickening as well as thinning of the photoreceptor layer in intermediate age-related macular degeneration. *Invest Ophthalmol Vis Sci*. 2013;54:1603–1612.

133. Gorczynska I, Srinivasan VJ, Vuong LN, et al. Projection OCT fundus imaging for visualising outer retinal pathology in non-exudative age-related macular degeneration. *Br J Ophthalmol*. 2009;93:603–609.

134. Shin I-H, Lee W-H, Lee J-J, Jo Y-J, Kim J-Y. Thickness of the macula, retinal nerve fibre layer, and ganglion cell-inner plexiform layer in age-related macular degeneration: The

135. Camacho P, Dutra-Medeiros M, Páris L. Ganglion cell complex in early and intermediate age-related macular degeneration: evidence by SD-OCT manual segmentation. *Ophthalmologica*. 2017;238:31–43.

136. Schlanitz FG, Baumann B, Kundi M, et al. Drusen volume development over time and its relevance to the course of age-related macular degeneration. *Br J Ophthalmol*. 2017;101:198–203.

137. Toy BC, Krishnadev N, Indaram M, et al. Drusen regression is associated with local changes in fundus autofluorescence in intermediate age-related macular degeneration. *Am J Ophthalmol*. 2013;156:532–542.e1.

138. Davis MD, Gangnon RE, Lee LY, et al. The Age-Related Eye Disease Study severity scale for age-related macular degeneration: AREDS Report No. 17. *Arch Ophthalmol*. 2005;123:1484–1498.

139. Guyatt GH, Oxman AD, Sultan S, et al. GRADE guidelines: 9. Rating up the quality of evidence. *J Clin Epidemiol*. 2011;64:1311–1316.

140. Rutter M. Beyond longitudinal data: causes, consequences, changes, and continuity. *J Consult Clin Psychol*. 1994;62:928–940.

Repeatability Study of Spectral Domain Optical Coherence Tomography. *Retina*. 2018;38:253–262.